

One mask to rule them all: Writing arbitrary intensity distributions by scanning a single illuminated spatially-random screen

David M. Paganin*

School of Physics and Astronomy, Monash University, Victoria 3800, Australia

(Dated: April 23, 2019)

Arbitrary intensity distributions may be written by transversely scanning a single spatially-random screen that is normally illuminated by spatially but not necessarily temporally uniform radiation or matter wave fields. The arbitrariness, of the written pattern, holds up to both (i) a spatial resolution that is dictated by the characteristic transverse length scale of the illuminated spatially random screen, and (ii) an additive constant. Two forms of the method are developed. The former assumes the distance between the illuminated random mask and the target plane to be sufficiently small that the effects of diffraction may be neglected. The latter accounts for the effects of Fresnel diffraction in the regime of large Fresnel number. Numerical simulations are provided for both variants of the method. The method may be parallelized, and is also suited to both magnifying and de-magnifying geometries. Possible applications include spatial light modulators and intensity projectors for those matter and radiation fields for which such devices do not exist, printing/micro-fabrication in both two and three spatial dimensions, and lithography.

I. INTRODUCTION

Synthesis and decomposition, of the functions used to model physical systems, often employs weighted superpositions of elements drawn from complete sets of basis functions [1]. Completeness holds irrespective of whether the problem under consideration is linear or non-linear. Basis-function sets may be localized or delocalized, depending on whether or not their support (or essential support) coincides with the entire volume under consideration, or some compact subset thereof. Localized bases include the Dirac-delta basis [2], wavelet bases [3], the pixel basis [4], tight-binding basis functions [5] etc. Polynomial bases [6], the Fourier basis [7], the Bloch-wave basis [8], the Hermite–Gauss basis [9], multipole-expansion bases [10], Green-function and other propagator-based constructs [11] all exemplify bases that are delocalized.

Another criterion for classifying complete bases, in the context of using them to construct functions that model physical systems, is the distinction between deterministic and random bases [12]. The previously-listed bases are all deterministic, as indeed are the majority of bases in common use. This is often related to the systematic manner in which such bases are constructed e.g. using standard approaches to solving key differential equations of mathematical physics [13]: modal approaches [14], eigenfunction expansions [15], approaches that exploit symmetries [16], perturbative expansions [17], multi-scale expansions [18] etc. Many but not all deterministic bases admit a natural ordering, e.g. via increasing eigenvalue, increasing modal order, increasing energy, increasing magnitude of momentum, increasing order of perturbation, increasing characteristic spatial or temporal scale etc.

All of the above is of course extremely well known. Focus attention, then, on the less-pervasive idea of *ran-*

dom basis functions [19, 20]. This may be motivated by the idea that randomly-chosen vectors in a suitable function space, will typically be linearly independent, and may therefore be considered as a basis [21]. Lack of orthogonality may be replaced with the weaker notion of orthogonality in expectation value [12] for random bases that become over-complete as sufficiently more members are added [22]. The ordering of elements in a random basis, e.g. of random vectors in the m -dimensional vector space \mathbb{R}^m , is not particularly meaningful even when it can be readily achieved e.g. by sorting the basis vectors in order of increasing norm. This typical lack of a meaningful order is somewhat related to over-completeness: if all elements of a random basis are generated by the same stochastic process, each such basis member is in some sense statistically equivalent, and therefore if enough such members are generated the set will become over-complete. The property of over-completeness is a superset of the property of completeness, and is not peculiar to random bases, as the well-known over-completeness of the coherent states (eigenfunctions of the destruction operator) shows [23]. Convergence rates, for random-basis expansions consisting of N terms, are often on the order of $N^{-1/2}$ in the L_2 -norm [21]. As with all truncated expansions, there is a trade-off between the expense of using a large number of terms to accurately represent a function in a random-basis-function expansion, versus the increased error inherent in using fewer terms [22].

Random bases are used in many fields of physics. For example, sequences of random orthonormal Hilbert space bases are used in the study of quantum chaos [24]. Both ghost imaging [25–30] and single-pixel cameras [31–33], when utilizing spatially random speckle fields, rely strongly on the random-basis concept [1, 12, 26, 27]. The field of compressed sensing [34] utilizes random bases in a rich variety of applications both within and beyond physics: see e.g. the review by Rani et al. [35] and references therein. Extensions beyond strictly physics-based applications include the use of random projections for

* david.paganin@monash.edu

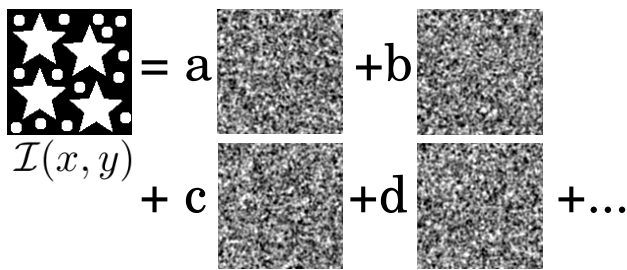


FIG. 1. Synthesizing an arbitrary image $\mathcal{I}(x, y)$ by superposing linearly independent speckle maps. $\mathcal{I}(x, y)$ is approximated as a multiplied by the first speckle image $\mathcal{M}_1(x, y)$, plus b multiplied by the second speckle image $\mathcal{M}_2(x, y)$, etc., where $a, b, \dots > 0$.

databases [36], facial recognition [37], machine learning [21], neural networks [20] and control theory [21].

Compressive sensing (albeit of a sparse or compressible signal) may be spoken of as “signal recovery from random projections” [34]. A variation of this theme, namely the question of signal *synthesis* using random projections, is the key topic of the present paper. In our imaging-optics context, the key idea is illustrated in Fig. 1. Here, we seek to express a specified intensity distribution $\mathcal{I}(x, y)$ as a linear combination of two-dimensional (2D) speckle maps. Each of these speckle maps is by assumption a different realization of a single spatially stationary ergodic stochastic process, such that (i) the mean and variance of the intensity are independent of position, and (ii) the intensity covariance is dependent only on coordinate differences. This last-mentioned condition is equivalent to the statement that the characteristic transverse speckle size l is independent of position in the field of view. One might expect the resolution of the resulting random-basis synthesis of $\mathcal{I}(x, y)$ to hold up to a spatial resolution governed by the speckle size l [1, 38, 39], provided enough elements are superposed.

Many motivations exist for pursuing optical schemes able to sculpt arbitrary specified intensity patterns via the transverse scanning of a single illuminated spatially-random mask. This is a means for creating spatial light modulators (SLMs) for radiation and matter wave fields, for which SLMs (i) do not exist, (ii) are prohibitively expensive, or (iii) do not have sufficiently high spatial resolution. Examples include the hard x-ray regime, as well as neutron beams and atomic beams. Reduced cost and complexity are another motivation, since compared to an SLM or data projector, the method is able to generate desired intensity patterns using only a steady source, a transversely scanned random screen, and an illumination plane/substrate. More remote potential applications include lithography and three-dimensional (3D) printing. Such potential future applications, together with unanticipated applications of the core idea developed in the present paper, provide some motivation for this work.

We close this introduction with a brief overview of the remainder of the paper. Section II develops the under-

pinning theory of scanning a single two-dimensional spatially random mask, that is illuminated by a spatially but not necessarily temporally uniform beam, so as to write an arbitrary specified pattern of intensity over a plane downstream of the illuminated mask. We firstly consider the case where the distance from the mask to the illumination plane is sufficiently small that the effects of diffraction may be neglected (Sec. II A). We then give a means by which such diffraction effects may be accounted for, provided certain specified conditions are met (Sec. II B). The theory is then illustrated with numerical simulations in Sec. III. A brief discussion, including possible future applications and extensions of the method, is given in Sec. IV. We conclude with Sec. V.

II. THEORY

Consider a spatially random mask having an intensity transmission function $\mathcal{M}(x, y)$ that is a spatially stationary, ergodic, isotropic, stochastic function of transverse coordinates x and y . The mask transverse dimensions $L \times L$ are assumed to be large with respect to the characteristic transverse length scale l of the speckled intensity distributions that arise over the exit surface of the mask, when uniformly illuminated by normally-incident statistically stationary partially coherent radiation or matter waves. Isotropy implies l to be independent of position (x, y) , while the assumptions of spatial stationarity and $L \gg l$ together imply that (i) spatial averages may be interchanged with ensemble averages; (ii) the statistical properties of the mask are independent of the origin of coordinates. Since ensemble and spatial averages are equal, both forms of average will be denoted by an overline, and used interchangeably.

Consider Fig. 2. Here, a statistically stationary source (e.g. of photons, neutrons, electrons, muons, pions, alpha particles, etc.) with intensity $I_0(t)$, uniformly illuminates a beam monitor that generates a signal

$$B(t) = \kappa I_0(t) \quad (1)$$

where $\kappa \geq 0$ is a real constant and t denotes time. The illumination need not be mono-energetic, and it may fluctuate with time, but it is assumed to be both spatially uniform and parallel to the optic axis z .

At the exit surface $z = 0$ of the spatially random mask, which has intensity transmission function $\mathcal{M}(x, y)$ with respect to the energy spectrum of the illuminating particles or fields, the intensity distribution will be

$$I(x, y, z = 0, t) = I_0(t)\mathcal{M}(x - \Delta x(t), y - \Delta y(t)). \quad (2)$$

Here, we have introduced time-dependent transverse shifts Δx and Δy in the x and y directions, respectively. Below it is shown how the exposure time for each transverse shift may be chosen so that the integrated intensity, over the illumination plane Π , can have any specified distribution (up to resolution l , and an additive constant).

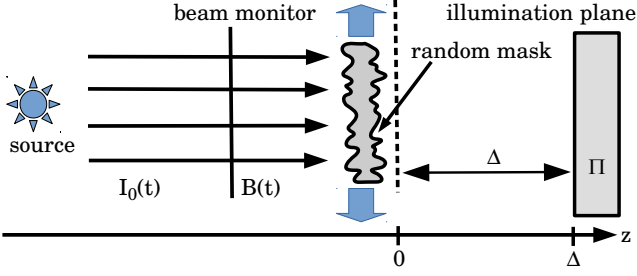


FIG. 2. Experimental setup for writing arbitrary intensity distributions over an illumination plane Π , given a single spatially random mask \mathcal{M} that is uniformly illuminated by a statistically stationary z -directed source. Here, $I_0(t)$ is the intensity of the illumination as a function of time t , Δ is the distance between the mask and the target plane, $B(t) \propto I_0(t)$ is a beam monitor signal, and $(\Delta x, \Delta y)$ is the transverse location of the mask. The mask is transversely translated during the exposure of Π . Alternatively, the mask may be kept fixed, with the illumination plane Π being transversely scanned.

Consider the set of N spatially random patterns:

$$\{\mathcal{M}_j(x, y)\} = \{\mathcal{M}(x - \Delta x_j, y - \Delta y_j)\}, \quad j = 1, 2, \dots, N, \quad (3)$$

where $(\Delta x_j, \Delta y_j)$, $j = 1, \dots, N$ is a sequence of $N \gg 1$ transverse displacement vectors, which are such that the distance between any two of these displacements is no smaller than the speckle size l :

$$\|(\Delta x_j - \Delta x_m, \Delta y_j - \Delta y_m)\| \geq l, \quad \forall j \neq m. \quad (4)$$

Here $\|(a, b)\| = \sqrt{a^2 + b^2}$ denotes the Euclidean norm of a 2D vector, $j, m = 1, \dots, N$ and $0 \leq \mathcal{M} \leq 1$. The condition in Eq. (4) ensures the masks in Eq. (3) are linearly independent. A cross-section through one realization of $\mathcal{M}_j(x, y)$ is sketched in Fig. 3(a), indicating the mean value $\bar{\mathcal{M}}$, characteristic speckle size l , and standard deviation σ in the transmission function. See also Fig. 3(b), which sketches a histogram of the mask transmission function. Note for later reference that we denote the mask with transmission function $\mathcal{M}_j(x, y)$ by \mathcal{M}_j .

The auto-covariance C of the ensemble of masks in Eq. (3), which spatial stationarity implies to be a function only of coordinate differences, is estimated via:

$$\begin{aligned} C(x - x', y - y') &= \frac{1}{N} \sum_{j=1}^N [\mathcal{M}_j(x, y) - \bar{\mathcal{M}}][\mathcal{M}_j(x', y') - \bar{\mathcal{M}}] \\ &\equiv \overline{[\mathcal{M}_j(x, y) - \bar{\mathcal{M}}][\mathcal{M}_j(x', y') - \bar{\mathcal{M}}]}. \end{aligned} \quad (5)$$

Here, (x, y) and (x', y') are any pair of points in the mask domain Ω , and N should be sufficiently large that the right side of Eq. (5) is indeed a good estimate for C . This auto-covariance will typically be a peaked function that decays to zero, which isotropy implies to be rotationally

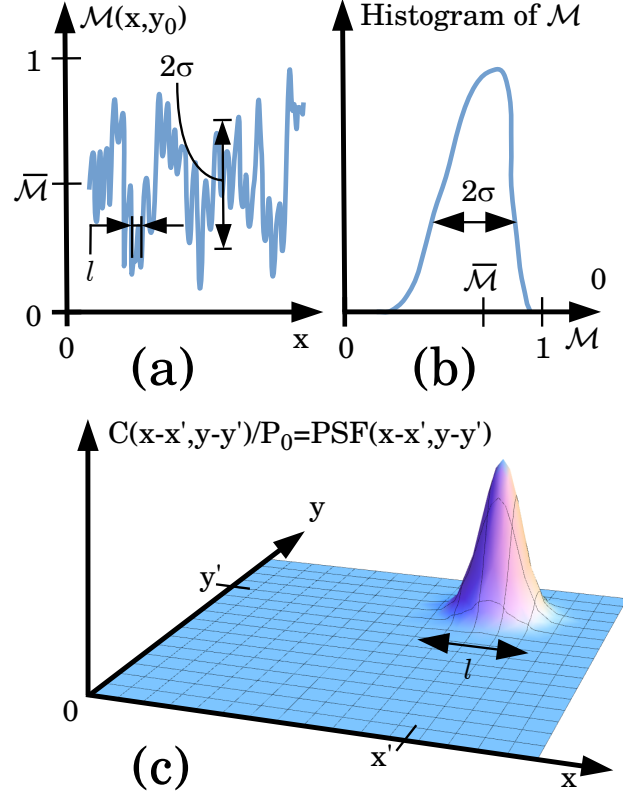


FIG. 3. (a) Slice through single realization of mask transmission function $\mathcal{M}_j(x, y)$, for fixed j and $y = y_0$. (b) Histogram of mask transmission function. (c) Auto-covariance $C(x - x', y - y')$ of ensemble of mask transmission functions, when normalized by its integral P_0 , is the point spread function $\text{PSF}(x - x', y - y')$ for synthesizing target intensity distributions by superposing realizations of the random mask.

symmetric, with diameter l given by the speckle size of the random mask. See Fig. 3(c).

Let P_0 be defined by

$$P_0 = \iint_{\Omega} C(x - x', y - y') dx dy, \quad (6)$$

which will be independent of (x', y') on account of spatial stationarity. Now, $C(x - x', y - y')/P_0$ has the properties expected for a point-spread function (PSF): it is narrow and peaked, with an area of unity [40]. Hence let

$$\text{PSF}(x - x', y - y') = C(x - x', y - y')/P_0, \quad (7)$$

so that Eq. (5) becomes a smoothed completeness relation [41]:

$$\begin{aligned} \text{PSF}(x - x', y - y') &= \frac{1}{NP_0} \sum_{j=1}^N [\mathcal{M}_j(x, y) - \bar{\mathcal{M}}][\mathcal{M}_j(x', y') - \bar{\mathcal{M}}]. \end{aligned} \quad (8)$$

Now let $\mathcal{I}(x, y)$ be a desired intensity distribution over the surface of the plane Π in Fig. 2. We separately consider the case where: (i) $\Delta = 0$; (ii) $\Delta > 0$.

A. Case #1: $\Delta = 0$

Multiply both sides of Eq. (8) by $\mathcal{I}(x', y')$, then integrate over x' and y' , to give:

$$\mathcal{I}(x, y) \star_2 \text{PSF}(x, y) = \frac{1}{NP_0} \sum_{j=1}^N (B_j - \bar{B}) [\mathcal{M}_j(x, y) - \bar{\mathcal{M}}]. \quad (9)$$

Here \star_2 denotes two-dimensional convolution,

$$B_j = \iint_{\Omega} \mathcal{I}(x, y) \mathcal{M}_j(x, y) dx dy \equiv \langle \mathcal{I}, \mathcal{M}_j \rangle \quad (10)$$

is the inner product (cross correlation) of the the j th mask with the desired intensity distribution $\mathcal{I}(x, y)$, and:

$$\bar{B} = \iint_{\Omega} \mathcal{I}(x, y) \bar{\mathcal{M}} dx dy = \frac{1}{N} \sum_{j=1}^N B_j. \quad (11)$$

To proceed further, observe that

$$\overline{(B_j - \bar{B})\bar{\mathcal{M}}} = \overline{(B_j - \bar{B})\bar{\mathcal{M}}} = 0. \quad (12)$$

Hence the term $\bar{\mathcal{M}}$ may be dropped from Eq. (9). This leaves a formula that is familiar from the different but related context of classical ghost imaging [1, 26, 27, 39]:

$$\mathcal{I}(x, y) \star_2 \text{PSF}(x, y) = \frac{1}{NP_0} \sum_{j=1}^N (B_j - \bar{B}) \mathcal{M}_j(x, y). \quad (13)$$

This random-basis expansion expresses the desired intensity distribution \mathcal{I} , up to a resolution of l implied by PSF smearing, as a linear combination of the ensemble of transversely displaced masks in Eq. (3) (cf. Fig. 1).

In a ghost-imaging context [30], the B_j would be *measured* “bucket signals” that may be used to reconstruct a ghost image of the left side of Eq. (13). In our context, we wish to synthesize the left side of Eq. (13) by *calculating* the required bucket coefficients B_j using Eq. (10) and then exposing each mask \mathcal{M}_j for a time proportional to $B_j - \bar{B}$. However, there is an important difference between the ghost-imaging application of Eq. (13), and the pattern-writing application we consider: $B_j - \bar{B}$ is a zero-mean random variable that can take on both negative and positive values. This conflicts with the fact that the exposure time for the j th mask, which should be proportional to $B_j - \bar{B}$, cannot be negative.

Hence adopt the following process:

1. Randomly select a set of $2N$ mask translation vectors $\{\Delta x_j, \Delta y_j\}$, $j = 1, 2, \dots, 2N$, which lie within the maximum range specified by $\Delta x_{\min} \leq \Delta x_j \leq \Delta x_{\max}$ and $\Delta y_{\min} \leq \Delta y_j \leq \Delta y_{\max}$ (see Fig. 4).
2. Calculate B_j for each translation vector using Eq. (10), and hence calculate $\bar{B} \equiv \bar{\mathcal{B}}$ using Eq. (11).

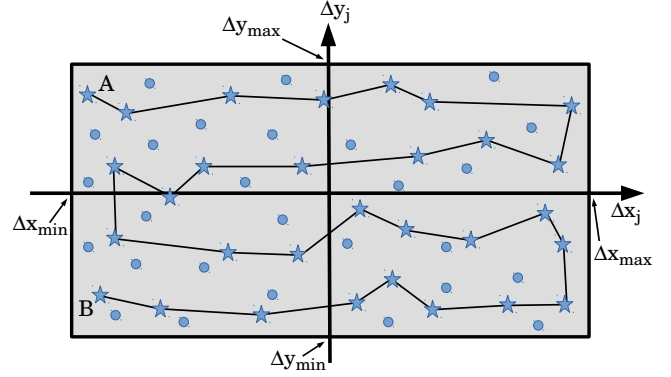


FIG. 4. A random sequence of transverse mask-displacement vectors $(\Delta x_j, \Delta y_j)$ is chosen. For each displacement, B_j is calculated using Eq. (10), together with the average $\bar{B} \equiv \bar{\mathcal{B}}$. Displacement vectors with $B_j > \bar{B}$, marked as stars, are retained and joined with a scan path AB . Displacement vectors with $B_j \leq \bar{B}$, marked with discs, are rejected.

3. Reject all translation vectors $\{\Delta x_j, \Delta y_j\}$ for which $B_j \leq \bar{B}$ (rejected vectors are marked as discs in Fig. 4, with accepted vectors as stars). This amounts to keeping only mask positions j' for which $\mathcal{M}_{j'}(x, y) \equiv \mathcal{M}(x - \Delta x_{j'}, y - \Delta y_{j'})$ has a cross correlation with the desired pattern $\mathcal{I}(x, y)$ that is larger than the average cross correlation.
4. Approximately N translation vectors will remain, with $N \ll A/l^2$ to ensure the spacing between vectors is greater than l , where $A = (\Delta x_{\max} - \Delta x_{\min})(\Delta y_{\max} - \Delta y_{\min})$. Join these together with an efficient path, giving the sequence of mask translations shown in Fig. 4. Note that, by construction, $B_{j'} - \bar{B} > 0$ for each of these masks.
5. If the spatially uniform incident illumination $I_0(t)$ (see Fig. 2) is independent of time t , expose each mask $\mathcal{M}_{j'}$ for a time $\tau_{j'}$ proportional to $B_{j'} - \bar{B} > 0$: thus $\tau_{j'} = \Xi(B_{j'} - \bar{B})$, where Ξ is a constant. If the spatially uniform incident illumination varies with time, as measured by the beam monitor signal in Eq. (1), expose each mask $\mathcal{M}_{j'}$ for a time $\tau_{j'}$ such that the total transmitted energy is proportional to $B_{j'} - \bar{B} > 0$.

With the above steps, and provided N is sufficiently large, Eq. (13) implies that the distribution of time-integrated energy density, over the plane Π in Fig. 2, will be equal to the required distribution $\mathcal{I}(x, y)$. This equality will hold up to (i) a multiplicative constant; (ii) isotropic transverse smearing over a length scale of l , due to the rotationally symmetric PSF associated with the process; (iii) an additive constant that is a consequence of Step #3 above. This last-mentioned property is an important limitation of the method.

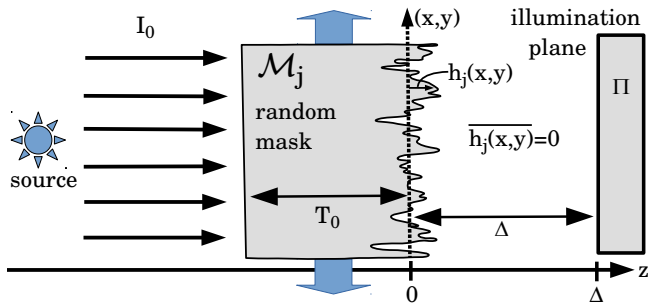


FIG. 5. Height profile for random mask composed of a single material. Here, the mask \mathcal{M}_j has projected thickness $T_0 + h_j(x, y)$, where $h(x, y)$ averages to zero under either or both of (i) ensemble average and (ii) spatial average.

B. Case #2: $\Delta \geq 0$

Now consider the case where Δ in Fig. 2 is sufficiently large that the effect of free-space diffraction cannot be ignored, due to propagation between the exit surface of the mask and the target surface Π .

Introduce additional assumptions that enable modelling of this free-space diffraction process: (i) Assume the illumination to be a quasi-monochromatic complex scalar field [42], which for concreteness we take to be hard x rays. (ii) Assume both mask and illumination to be such that the projection approximation is valid [43]. This is a high-energy approximation that amounts to assuming the mask to be sufficiently slowly varying, and the illumination of sufficiently high energy, that the streamlines of the current density within the mask are very close to parallel to the optic axis. (iii) Assume the mask to be made of a single material with linear attenuation coefficient μ , and real refractive index $n = 1 - \delta$ [43]. (iv) Assume the Fresnel number

$$N_F \equiv l^2/(\lambda\Delta), \quad (14)$$

corresponding to Fresnel diffraction of paraxial waves with wavelength λ , to obey $N_F \gg 1$. Stated differently, assume Δ is small enough that the plane Π is in the near field of the mask [43] (see Fig. 2). (v) Assume the incident illumination intensity I_0 to be time-independent. This last assumption is easily dropped, but has been included for both simplicity and clarity.

The above assumptions enable use of a finite-difference form of the transport-of-intensity equation [44], namely the continuity equation expressing local energy conservation for the parabolic equation of paraxial wave optics [45]. This gives the following estimate for the intensity distribution, due to illumination of the j th state of the mask, over the target surface Π in Fig. 2 [46]:

$$I_j(x, y, z = \Delta) = I_0 \left(1 - \frac{\Delta\delta}{\mu} \nabla_{\perp}^2 \right) \exp[-\mu T_j(x, y)]. \quad (15)$$

Here, ∇_{\perp}^2 is the Laplacian in the xy plane, the projected

thickness $T_j(x, y)$ of the j th state of the mask is:

$$T_j(x, y) = T_0 + h_j(x, y), \quad (16)$$

T_0 is a constant offset mask thickness and $h_j(x, y)$ is a stochastic fluctuation that (i) ensemble averages to zero at every point (x, y) in the domain Ω of the mask; (ii) spatially averages to zero for every realization j of the mask (see Fig. 5). Note that the projected thickness in Eq. (16) may be produced by either or both of (i) surface roughness and (ii) density fluctuations within the mask. The former case is illustrated in Fig. 5.

Now assume the absorption of the mask to be weak, so that the exponential in Eq. (15) can be Taylor expanded to first order in its argument. To first order in Δ , this gives the following expression for the auto-covariance of the intensity at the exit surface of the mask:

$$\begin{aligned} & \overline{[I_j(x, y, z = \Delta) - \bar{I}][I_j(x', y', z = \Delta) - \bar{I}]} \\ & = I_0^2 (\mu^2 - 2\Delta\delta\mu\nabla_{\perp}^2) \overline{h_j(x, y)h_j(x', y')}. \end{aligned} \quad (17)$$

Here,

$$\begin{aligned} \bar{I} & = I_0 \overline{\left(1 - \frac{\Delta\delta}{\mu} \nabla_{\perp}^2 \right) \exp\{-\mu[T_0 + h_j(x, y)]\}} \\ & = I_0 \overline{\exp\{-\mu[T_0 + h_j(x, y)]\}} \\ & \approx I_0 \overline{1 - \mu[T_0 + h_j(x, y)]} \\ & = I_0 [1 - \mu T_0 - \mu \overline{h_j(x, y)}] \\ & = I_0 (1 - \mu T_0). \end{aligned} \quad (18)$$

Note that Eq. (18) makes the intuitive statement that Fresnel diffraction does not change the average transverse energy density of the propagating radiation. Note also, that the Laplacian in Eq. (17) acts only on the (x, y) coordinate, and not on (x', y') .

Denote the intensity auto-covariance by

$$\begin{aligned} & C_I(x - x', y - y', z = \Delta) \\ & \equiv \overline{[I_j(x, y, z = \Delta) - \bar{I}][I_j(x', y', z = \Delta) - \bar{I}]} \end{aligned} \quad (19)$$

and the height auto-covariance by

$$\begin{aligned} C_h(x - x', y - y') & = \overline{[h_j(x, y) - \bar{h}][h_j(x', y') - \bar{h}]} \\ & = \overline{h_j(x, y)h_j(x', y')}, \end{aligned} \quad (20)$$

where the last equality follows from $\bar{h} = 0$. Upon transforming from Cartesian coordinates $(x - x', y - y')$ to plane polar coordinates (R, Θ) , and dropping explicit Θ dependence due to rotational symmetry, Eq. (17) becomes:

$$C_I(R, z = \Delta) = I_0^2 (\mu^2 - 2\Delta\delta\mu\nabla_{\perp}^2) C_h(R). \quad (21)$$

As was the case in Sec. II A, promote the intensity covariance $C_I(R)$ to the status of a PSF by normalizing to unity using Eq. (7). Thus

$$\text{PSF}(R, z = \Delta) = \tilde{P}_0^{-1} C_I(R), \quad (22)$$

where the Δ -independent normalization constant

$$\tilde{P}_0 \equiv \iint_{\Omega} C_I(R) R dR d\Theta = 2\pi I_0^2 \mu^2 \int_0^{\infty} R C_h(R) dR \quad (23)$$

ensures that $\iint \text{PSF}(R, z = \Delta) R dR d\Theta = 1$ for all $\Delta \geq 0$. Note that a boundary term has been discarded in deriving Eq. (23), by applying the Gauss divergence theorem to $\iint \nabla_{\perp}^2 C_h(R) R dR d\Theta$ and assuming that $C_h(R)$ decays to zero faster than $1/R$. Thus Eq. (21) becomes:

$$\text{PSF}(R, z = \Delta) = \frac{I_0^2 \mu^2}{\tilde{P}_0} \left(1 - \frac{2\Delta\delta}{\mu} \nabla_{\perp}^2 \right) C_h(R). \quad (24)$$

By comparing the $\Delta = 0$ case of Eq. (24) with the case for $\Delta \in (0, \Delta_{\max})$, where Δ_{\max} is the largest mask-to-target-plane propagation distance consistent with the key assumption that the Fresnel number be much larger than unity, we see that

$$\text{PSF}(R, z = \Delta) = \mathcal{L} \text{PSF}(R, z = 0). \quad (25)$$

Here, \mathcal{L} is the linear differential operator:

$$\mathcal{L} = 1 - \frac{2\Delta\delta}{\mu} \nabla_{\perp}^2. \quad (26)$$

Note that operators will always be considered to act on all objects that appear to their right, so that e.g. $\mathcal{U}\mathcal{V}f \equiv \mathcal{U}[\mathcal{V}(f)]$ for operators \mathcal{U}, \mathcal{V} and functions f . Note also that the Fourier derivative theorem gives the following Fourier representation for \mathcal{L} [43, 46]

$$\mathcal{L} = \mathcal{F}^{-1} \left[1 + \frac{2\Delta\delta}{\mu} (k_x^2 + k_y^2) \right] \mathcal{F}, \quad (27)$$

where \mathcal{F} denotes Fourier transformation with respect to x, y , \mathcal{F}^{-1} denotes the corresponding inverse Fourier transformation, and (k_x, k_y) are Fourier variables dual to (x, y) . We have used a Fourier-transform convention in which the Fourier derivative theorem takes the form where differentiation with respect to x or y in (x, y) space corresponds to multiplication by ik_x or ik_y in (k_x, k_y) space. In this Fourier representation, the inverse to \mathcal{L} is the Lorentzian low-pass Fourier filter

$$\mathcal{L}^{-1} = \mathcal{F}^{-1} \frac{1}{1 + 2\Delta\delta\mu^{-1}(k_x^2 + k_y^2)} \mathcal{F}. \quad (28)$$

A convolution representation of \mathcal{L}^{-1} is readily obtained, with the aid of both the convolution theorem of Fourier analysis and a table of Hankel transforms [7], to give

$$\mathcal{L}^{-1} = \frac{K_0(r/\sqrt{\zeta})}{2\pi\zeta} \star_2, \quad \zeta \equiv \frac{2\delta\Delta}{\mu}. \quad (29)$$

Here, K_0 is the modified Bessel function of the second kind and zeroth order.

Next, recall the fact that the definition of the convolution integral implies

$$\mathcal{K}(f \star g) = (\mathcal{K}f) \star g = f \star (\mathcal{K}g), \quad (30)$$

for any linear operator \mathcal{K} and any functions f, g that are sufficiently well behaved that the orders of application of (i) integration and (ii) \mathcal{K} can be interchanged. Now, if we were to use $\text{PSF}(R, z = \Delta)$ in the scheme outlined in the previous subsection, which neglects the effects of non-zero Δ , Eq. (13) shows that the target plane would register the intensity distribution $\mathcal{I}(x, y) \star_2 \text{PSF}(x, y, z = \Delta)$. Making use of Eqs. (25) and (30), and reverting back to Cartesian coordinates, we see that this registered intensity distribution may be written as:

$$\begin{aligned} \mathcal{I}(x, y) \star_2 \text{PSF}(x, y, z = \Delta) &= \mathcal{I}(x, y) \star_2 [\mathcal{L} \text{PSF}(x, y, z = 0)] \\ &= [\mathcal{L} \mathcal{I}(x, y)] \star_2 \text{PSF}(x, y, z = 0). \end{aligned} \quad (31)$$

The presence of \mathcal{L} in the final line of Eq. (31) implies that the wrong pattern will be written, if one were to apply the scheme of Sec. II A without modification: up to smearing by $\text{PSF}(x, y, z = 0)$, the pattern that is written is $\mathcal{L} \mathcal{I}(x, y)$ rather than the required pattern of $\mathcal{I}(x, y)$.

The required modification is to make the replacement

$$\mathcal{I}(x, y) \rightarrow \mathcal{L}^{-1} \mathcal{I}(x, y) \quad (32)$$

in Eq. (31), to obtain

$$\begin{aligned} [\mathcal{L}^{-1} \mathcal{I}(x, y)] \star_2 \text{PSF}(x, y, z = \Delta) &= \mathcal{L}^{-1} \mathcal{I}(x, y) \star_2 [\mathcal{L} \text{PSF}(x, y, z = 0)] \\ &= [\mathcal{L} \mathcal{L}^{-1} \mathcal{I}(x, y)] \star_2 \text{PSF}(x, y, z = 0) \\ &= \mathcal{I}(x, y) \star_2 \text{PSF}(x, y, z = 0). \end{aligned} \quad (33)$$

This is the key result of the present paper, since the last line of Eq. (33) is the required pattern $\mathcal{I}(x, y)$, smeared by the ‘‘contact’’ PSF.

Hence, when Δ in Fig. 2 is large enough that its effects cannot be neglected, one can obtain a desired intensity distribution over the target plane using the setup in Fig. 2, with exactly the same sequence of five steps in Sec. II A, via the single modification that the replacement in Eq. (32) is made. Note that, in the limit $\Delta \rightarrow 0$, we have $\mathcal{L}^{-1} \rightarrow 1$, so that the formalism of the present sub-section is a generalization of that in Sec. II A.

We close this sub-section by noting that the asymptotic behavior (see e.g. Eq. (10.25.3) in Olver et al. [47])

$$K_0 \left(\frac{r}{\sqrt{\zeta}} \right) \sim \sqrt{\frac{\pi\sqrt{\zeta}}{2r}} \exp \left(-\frac{r}{\sqrt{\zeta}} \right), \quad \frac{r}{\sqrt{\zeta}} \rightarrow \infty, \quad (34)$$

of the convolution kernel in Eq. (29) ensures that, when \mathcal{L}^{-1} acts on a compactly supported distribution such as the desired target pattern $\mathcal{I}(x, y)$, the result retains the property of compact support.

C. Remark

Many models for rough surfaces, such as that of Sinha et al. [48], could be introduced for $C_I(R)$ and $C_h(R)$ in Sec. II B. For simplicity, consider the Gaussian form

$$C_h(R) = \sigma_h^2 \exp[-(R/\xi)^2]. \quad (35)$$

Here, σ_h^2 is the variance of the height distribution sketched in Fig. 5 (see also Eq. (16)), and ξ is the characteristic transverse length scale over which the rough height profile is correlated. The same quantity ξ is equal to the characteristic transverse speckle size l for any particular realization of Eq. (15). It is also equal to the spatial resolution with which the scheme of the present paper allows the desired pattern $\mathcal{I}(x, y)$ to be written.

For the model in Eq. (35), Eq. (24) becomes the family of normalized PSF curves:

$$\begin{aligned} \text{PSF}(R, z = \Delta) & \quad (36) \\ &= \frac{1}{\pi\xi^2} \left\{ 1 - \frac{2}{\pi} \frac{\delta}{\beta} N_F^{-1} \left[\left(\frac{R}{\xi} \right)^2 - 1 \right] \right\} \exp[-(R/\xi)^2]. \end{aligned}$$

Here, $\beta = \mu/(2k)$, where $k = 2\pi/\lambda$ is the wave-number corresponding to vacuum wavelength λ , and the Fresnel number is $N_F = \xi^2/(\lambda\Delta)$.

Three different instances of these PSFs are sketched in Fig. 6, corresponding to three different values for the dimensionless parameter

$$\tau \equiv \frac{\delta}{\beta} N_F^{-1} = \frac{\delta\lambda\Delta}{\beta\xi^2}. \quad (37)$$

When $\tau = 0$, corresponding to $\Delta = 0$, one has a Gaussian PSF. However, when $\tau > 0$, the central positive peak in the PSF develops a negative ‘‘moat’’ due to Fresnel diffraction through the distance Δ . Note that the choice of non-zero τ values illustrated in Fig. 6 has been guided by the facts that (i) the Fresnel number must be much greater than unity for Eq. (15) to be valid; (ii) typical values for δ/β are in the range of 100 – 1000 for many materials in the hard x-ray regime. The ‘‘moats’’ evident in the $\tau \neq 0$ PSFs of Fig. 6, which are a special case of similar behavior for the more general expression in Eq. (25), are consistent with similar features seen in several papers calculating experimental x-ray speckle correlation functions in a different context, namely x-ray phase contrast velocimetry [49–51].

III. SIMULATIONS

The cases of zero and non-zero Δ (see Fig. 2) are numerically modelled in Secs. III A and III B, respectively.

A. Simulations for $\Delta = 0$

To simulate a spatially-random mask, a 1024×1024 pixel array was populated with pseudo-random real numbers uniformly distributed between zero and unity. This white-noise array was then smoothed via convolution with a rotationally-symmetric Gaussian with standard deviation equal to one pixel, giving a speckle width of $l = 2$ pixels. The resulting random array of gray-scale values was taken to be the transmission function $\mathcal{M}(x, y)$

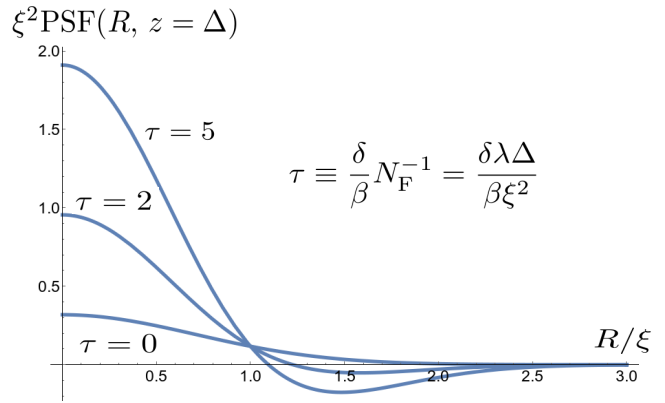


FIG. 6. Three examples of the Δ -dependent PSF given in Eq. (36), for different values of the dimensionless parameter τ defined in Eq. (37). The case $\tau = 0$ corresponds to a Gaussian PSF associated with $\Delta = 0$ in Fig. 2, while non-zero τ values of 2 and 5 correspond to non-zero Δ .

of the mask, denoted by $\mathcal{M}(x, y)$ in Eq. (2). A 128×128 pixel sub-region of this mask is shown in Fig. 7(a), with the corresponding histogram of transmission-level values in Fig. 7(b). The five steps in Sec. II A were then followed:

1. The simulated 1024×1024 mask was randomly transversely displaced to M different locations, to generate an ensemble of linearly-independent mask transmission functions corresponding to Eq. (3). Each such mask had a field-of-view of 128×128 pixels, with randomly chosen location within the full 1024×1024 pixel mask. For simplicity, periodic boundary conditions were assumed.
2. The target image was taken to be the 128×128 pixel binary image $\mathcal{I}(x, y)$ in Fig. 7(c). Using this motif, B_p for was calculated for each translation vector using Eq. (10), with the integral being estimated via addition of pixel values. No transverse length scale needed to be specified in these simulations, hence (i) simulated bucket values were only calculated up to an unspecified multiplicative constant; (ii) there are no spatial scale bars in Fig. 7. Next, $\bar{B} \equiv \bar{B}$ was calculated using Eq. (11).
3. Rejection of all mask translation vectors for which $B_j \leq \bar{B}$ implied that approximately half of the M mask positions were utilized.
4. For the purposes of simulation, the order in which the masks were exposed was irrelevant, hence there was no need to calculate a suitable trajectory of mask positions such as that shown in Fig. 4.
5. Each retained mask was multiplied by $B_j - \bar{B}$, corresponding to exposure of the illuminated surface for

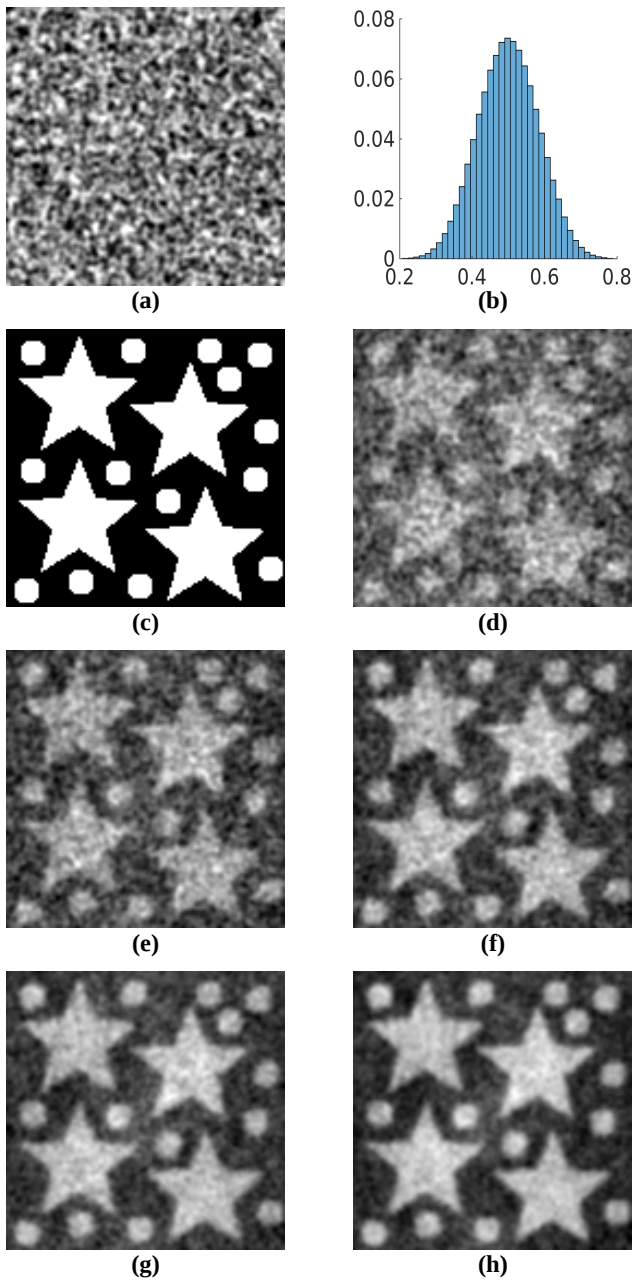


FIG. 7. Simulations for scanning a single spatially random mask, to create a desired intensity distribution, for the case $\Delta = 0$ (see Fig. 2). (a) 128×128 pixel sub-region of transmission function of simulated 1024×1024 pixel mask \mathcal{M} ; (b) Histogram of gray levels for \mathcal{M} , with vertical axis scaled to be a probability for each bin, with the whole 1024×1024 map having mean $a = 0.50$, standard deviation $\sigma = 0.083$ and mask contrast $\kappa_{\text{mask}} = 2\sigma/a = 33\%$; (c) 128×128 pixel target image $\mathcal{I}(x, y)$, consisting of values of either zero or unity; (d) Intensity corresponding to $M = 10^4$ mask positions, of which $M' = 4,979$ are used, giving a pattern with contrast $\kappa = 1.03\%$; (e) $M = 2 \times 10^4$, $M' = 10,042$, $\kappa = 0.95\%$; (f) $M = 5 \times 10^4$, $M' = 25,058$, $\kappa = 0.89\%$; (g) $M = 10^5$, $M' = 49,978$, $\kappa = 0.87\%$; (h) $M = 2 \times 10^5$, $M' = 100,197$, $\kappa = 0.86\%$. All gray-scale images displayed on linear scale from black (minimum value) to white (maximum value).

a time proportional to $B_j - \bar{B}$, under the assumption that $I_0(t)$ is independent of time in Eq. (1). The resulting weighted masks were then summed.

The synthesized intensity distributions due to $M = 10^4, 2 \times 10^4, 5 \times 10^4, 10^5, 2 \times 10^5$ mask positions (prior to the rejection of approximately half of the mask positions in Step #3) are shown in Fig. 7(d-h) respectively. The contrast κ of all synthesized intensity distributions, which is on the order of 1%, may be compared to the speckle-mask contrast $\kappa_{\text{mask}} = 33\%$. Again, such low contrast is a key limitation of the method.

B. Simulations for $\Delta > 0$

Consider a spatially random mask made from a copper sheet with one roughened surface (see Fig. 5). The following simulations assume this to be illuminated by normally incident quasi-monochromatic x rays of energy 17.2 keV (wavelength 0.72 Å). The corresponding optical parameters are $\delta = 5.8 \times 10^{-6}$ and $\beta = 2.7 \times 10^{-7}$ [52]. Assume a characteristic transverse length scale for the roughness of $l = \xi = 20 \mu\text{m}$. Since the Fresnel number N_F must be much greater than unity for our analysis to be valid, set $N_F = 5$ in Eq. (14) and solve for the mask-to-substrate distance Δ to give $\Delta = l^2/(\lambda N_F) \approx 1\text{m}$. This distance is reasonable and practical for synchrotron and laboratory sources of hard x rays. Setting the aspect ratio of the roughness to 0.05 estimates the standard deviation of the stochastic height profile $h_j(x, y)$ to be approximately $\sigma_h = 1 \mu\text{m}$ (cf. Eq. (35)). The same “filtered white noise” approach, as in Sec. III A, was used to simulate one spatially random mask with projected thickness $T(x, y)$ consistent with the above parameters (see Eq. (16)). A 1024×1024 pixel array was again used for the entire random mask, with the same 128×128 pixel target intensity distribution as in Fig. 7(c). The physical width and height of each pixel was $10 \mu\text{m}$. The mask substrate thickness T_0 did not need to be specified since it only affects all outputs by a multiplicative constant.

The projection approximation [43, 46] was used to calculate the complex x-ray wave field at the exit surface of the mask, as a function of the modelled projected thickness, using the parameters given above. The Fourier representation of the Fresnel propagator was then used to calculate the propagated intensity over the target plane. The propagated speckle field for one position of the mask, corresponding to $\Delta = 1\text{m}$ in Fig. 2, is shown in Fig. 8(a). Compared to the non-propagated speckle in Fig. 7(a), Fig. 8(a) has additional fine detail due to propagation-based phase contrast [53–55] as quantified by the Laplacian term in Eq. (15). When no correction was made for the non-zero Δ , the output maps in Figs. 8(b-d) were obtained, corresponding respectively to $M = 10^4, 5 \times 10^4, 2 \times 10^5$ pre-rejection mask positions. The high-pass filtration of $\mathcal{I}(x, y)$ by \mathcal{L} , as predicted in Eqs. (27) and (31), is evident as the black-white halos

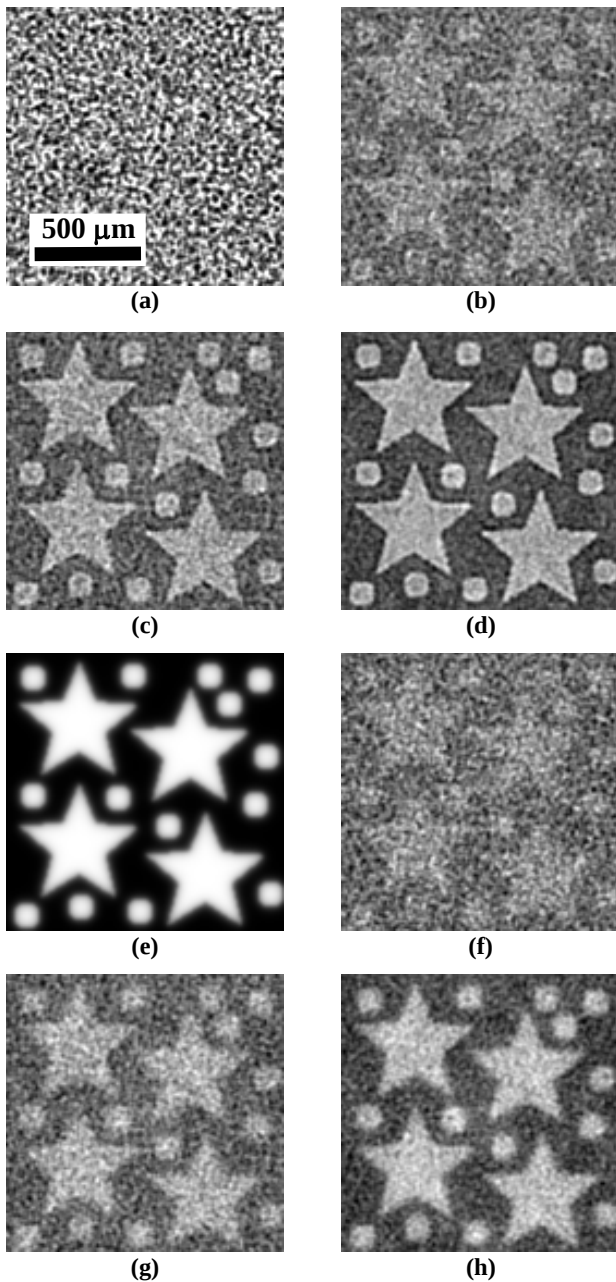


FIG. 8. Simulations for $\Delta > 0$ (see Fig. 2). (a) 128×128 pixel sub-region of 1024×1024 pixel propagated intensity distribution due to mask transmission function described in main text, with whole map having mean $a = 0.8249$, standard deviation $\sigma = 0.0992$ and mask contrast $\kappa_{\text{mask}} = 2\sigma/a = 24\%$; (b) Intensity corresponding to $M = 10^4$ mask positions, of which $M' = 5,011$ are used, giving a pattern with contrast $\kappa = 0.52\%$, no propagation correction; (c) $M = 5 \times 10^4$, $M' = 24,780$, $\kappa = 0.35\%$, no propagation correction; (d) $M = 2 \times 10^5$, $M' = 99,246$, $\kappa = 0.31\%$, no propagation correction; (e) $\mathcal{L}^{-1}\mathcal{I}(x, y)$; (f) $M = 10^4$, $M' = 5,110$, $\kappa = 0.25\%$, with propagation correction; (g) $M = 5 \times 10^4$, $M' = 25,326$, $\kappa = 0.32\%$, with propagation correction; (h) $M = 2 \times 10^5$, $M' = 101,157$, $\kappa = 0.27\%$, with propagation correction; All gray-scale images displayed on linear scale from black (minimum value) to white (maximum value).

at the edges of each feature in the synthesized motifs, together with the fact that the background is paler than was the case in Fig. 7. Such halos may also be thought of as due to the “moat” surrounding the $\tau > 0$ PSFs in Fig. 6. Notwithstanding these distortions, the images in Figs. 8(b,c,d) look sharper than their counterparts in Figs. 7(d,e,h), since Eq. (15) is mathematically identical in form to Laplacian based unsharp-mask image sharpening [56, 57], albeit in an over-sharpened regime where the previously mentioned black-white halo surrounds feature edges. To correct for the formation of such artefacts, the target motif was transformed according to the replacement given in Eq. (32), using the convolution representation (Eq. (29)) of the smoothing operator \mathcal{L}^{-1} . The characteristic transverse length scale $\sqrt{\zeta}$ for the modified Bessel function smoothing kernel was obtained from the previously stated values of $\Delta, \delta, \mu = 2k\beta$ to be $\sqrt{\zeta} = \sqrt{2\delta\Delta/\mu} = 15.7\mu\text{m} \approx 1.5$ pixels (cf. Eq. (29)). The resulting smoothed motif $\mathcal{L}^{-1}\mathcal{I}(x, y)$ is shown in Fig. 8(e). The corresponding written images in Figs. 8(f-h), which correspond to $M = 10^4, 5 \times 10^4, 2 \times 10^5$ pre-rejection masks respectively, were not distorted by a black-white halo. Note that, while there may appear to be a faint remaining halo when inspecting Figs. 8(f-h), this is not in fact that case, but is rather due to the Mach band phenomenon of physiological optics [58, 59].

IV. DISCUSSION

Specific means for generating the spatially random patterns, required for the method, are as follows. The ground glass plate, illuminated by a laser, is the classic means to generate spatially random patterns using visible light [60]. Note, however, that it would need to be sufficiently thin for the method of Sec. IIB to be applied. For hard x rays, suitable spatially random screens include wood [54], graphite [61], paper [62], sandpaper [63], amorphous boron powder [64], porous nano-crystalline beryllium [65], slabs of ground glass spheres [39], and structures formed via speckle lithography on black silicon [66]. For transmission electron microscopy, amorphous carbon films [67] or metallic glasses [68] may be used. Spatially random neutron distributions may be obtained via illumination of metallic powders [69], slabs of sand and other granular materials [70]. In all of the above cases propagation-based phase contrast, due to non-zero Δ in Fig. 2, may be employed to increase the contrast of the speckles—see, respectively, Bremmer [71], Aloisio et al. [63], Cowley [8] and Allman et al. [72], for the cases of visible light, hard x rays, electrons and neutrons.

Irrespective of the type of radiation or matter wave-field that is used, there may be contexts such as lithography, where non-zero Δ is unavoidable. Also, there may be cases where non-zero Δ is useful, such as when propagation-based phase contrast [53–55, 72, 73] (also known as out-of-focus contrast in visible-light [71] and electron-optical [8] contexts) is used to yield a high-

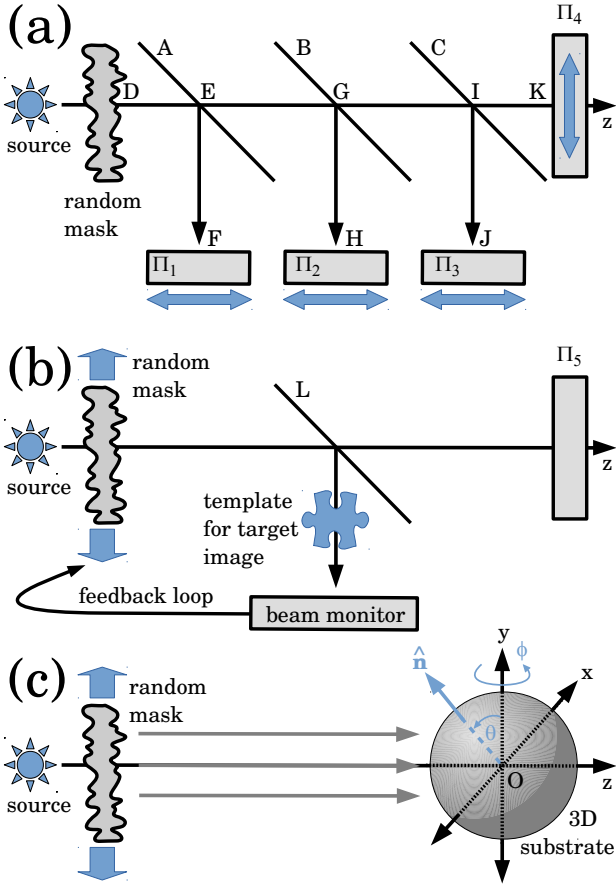


FIG. 9. (a) Parallel version of the scheme sketched in Fig. 2. (b) All-optical version. (c) 3D-printing version.

visibility spatially random pattern. Another context where non-zero Δ is unavoidable is the parallel version of this paper’s central scheme, shown in Fig. 9(a). Here, a single stationary spatially random mask, illuminated by a steady source, illuminates the plane Π_1 via beam-splitter A , the plane Π_2 via beam-splitter B , and the plane Π_3 via beam-splitter C . Plane Π_4 corresponds to the undeviated attenuated beam. Varying exposure times for each target plane are obtained by transversely displacing the target planes rather than the mask. For planes Π_1, \dots, Π_4 , the respective propagation distances are $\Delta = d(DEF), d(DGH), d(DIJ), d(DK)$, where $d(DEF)$ denotes the distance from D to E to F , etc. Up to a resolution governed by the speckle size of the mask, and an additive constant, arbitrary intensity distributions $\mathcal{I}_j(x, y)$ can be registered over the planes Π_j , where $j = 1, 2, \dots$, using the scheme for non-zero Δ in Sec. II B.

How many linearly independent masks may be generated by spatially translating a single spatially random mask in the xy direction, as well as rotating it about the z axis? A crude lower bound \mathcal{N} for this number may be obtained under the assumptions that (i) the field-of-

view of $\mathcal{I}(x, y)$ is significantly smaller than the size of the mask; (ii) the field-of-view of $\mathcal{I}(x, y)$ is much larger than the speckle size $l = \xi$; (iii) half of the masks will need to be rejected since their cross-correlation with the desired pattern will be less than the mean cross-correlation (cf. Step #3 in Sec. II A). Thus:

$$\mathcal{N} \geq \frac{A^2 B}{2l^3}. \quad (38)$$

Here, A^2 is the area of the spatially random mask and B^2 is the area of the pattern $\mathcal{I}(x, y)$ that one seeks to write to a spatial resolution of $l \ll B$. Equation 38 corresponds to $(A/l) \times (A/l)$ transverse displacements corresponding to two orthogonal directions, for each of B/l rotation directions about the optic axis z . If translations but not rotations are permitted, we would instead have

$$\mathcal{N}' \approx \frac{A^2}{2l^2}. \quad (39)$$

For example, the simulations of Sec. III had $A = 8B$ (corresponding to a random mask with width and height that are both 8 times as large as the width and height of the desired pattern \mathcal{I}) and $B = 64l$ (since the width of one speckle in the mask is twice the one-pixel standard deviation of the Gaussian filter used to smooth the input 128×128 pixel white noise map), so that Eq. (38) gives $\mathcal{N} \geq 8 \times 10^6$ linearly independent masks that may be generated from a single mask, using only transverse displacement and rotation. Equation 39, which does not consider mask rotations, gives $\mathcal{N}' \approx 1 \times 10^5$; this is consistent with the maximum number of masks used in the simulations.

An all-optical version of the method is possible: see Fig. 9(b). Assume time-independent spatially uniform illumination I_0 , for simplicity. The all-optical setup is identical to that for ghost imaging using a random screen [26, 27, 39], with three changes: (i) the illumination-pattern detection plane is replaced with the target illumination plane Π_5 ; (ii) the object to be imaged is now replaced with a template of the pattern that is to be imprinted on plane Π_5 ; (iii) a feedback loop returns the average-subtracted beam-monitor signal $\bar{B} = B - \bar{B}$ back to the mask translation stage, illuminating Π_5 for a time proportional to \bar{B} , for each mask position. In accord with Step #3 of the core scheme (see Sec. II A), only mask positions for which $\bar{B} > 0$ are kept; all such positions can be determined before exposure of Π_5 . The average bucket signal \bar{B} should be determined prior to any illumination of the substrate, via a random series of mask positions as chosen in Step #1 of the core scheme (see also Fig. 4). This all-optical setup is very closely related to the Hadamard-transform scheme for ghost imaging using the human eye, utilising a digital micro-mirror device, recently published by Boccolini et al. [74]; see also Wang et al. [75, 76], and references therein.

While the present paper has been developed in 2D, it may be applied to 3D. See Fig. 9(c). This conceptually combines a “tomography in reverse” approach to 3D

printing [77], with ghost tomography [78, 79], to give the idea of illuminating a three-dimensional dose-sensitive substrate from many orientations, using speckles created by a single spatially random mask with a number of different transverse positions, to create an arbitrary desired three-dimensional distribution of dose, $\rho(x, y, z)$, up to the usual additive constant. Thus (cf. Eq. (13) in Kingston et al. [79]):

$$\rho(x, y, z) \propto \overline{\overline{\tilde{B}_j^{(\theta, \phi)} \mathcal{A} \mathcal{P}_{\theta, \phi}^{-1} \mathcal{L}^{-1} \mathcal{M}_j(x_{\theta, \phi}, y_{\theta, \phi})}}. \quad (40)$$

Here, (x, y, z) are Cartesian coordinates with origin O at the center of the illuminated spherical substrate, the double overline indicates an ensemble average over both transverse mask positions and substrate orientations $\{\hat{\mathbf{n}}\}$, the set of unit vectors $\{\hat{\mathbf{n}}\}$ with spherical polar angular coordinates (θ, ϕ) is uniformly randomly distributed over the unit sphere centered at O , each member of the set $\{\tilde{B}_j^{(\theta, \phi)}\}$ is proportional to background-subtracted illumination times in accord with Step #5 of the core scheme, $\mathcal{P}_{\theta, \phi}^{-1}$ is the tomographic back-projection operator corresponding to the direction (θ, ϕ) , $(x_{\theta, \phi}, y_{\theta, \phi})$ are Cartesian coordinates in the plane perpendicular to the back-projection direction, and \mathcal{A} is a high-pass filter (e.g. the Ramachandran-Lakshminarayanan filter [80] or a related filter adapted to the fact that the scheme of Fig. 9(c) rotates about two axes rather than one axis) that transforms the back-projection operator into the filtered back-projection operator [81]. Note that there may be some cancellation between the high-pass filter \mathcal{A} and the low-pass filter \mathcal{L}^{-1} , as noted by Gureyev et al. [82] in a different but related context. Such cancellation arises from the similarity between the “peak plus moat” morphology of the point spread function in Fig. 6, and a similar morphology for the impulse response function associated with tomographic back projection (see e.g. Fig. 3.12 in the book by Kak and Slaney [81]).

We close this discussion with several miscellaneous remarks: (i) The method is a form of scanned-probe patterning which “writes with many pens in parallel”, i.e. using a delocalized spatially random “pen bundle” rather than the more conventional highly spatially localized “pen”. This parallels a distinction between conventional scanning-probe imaging and classical ghost imaging: the former scans a localized probe [83] to form an image with resolution governed by the probe size, while the latter scans a delocalized spatially-random mask to similar effect but with resolution governed by the speckle size of the scanned spatially random probe [1, 38, 39]. (ii) The method may be viewed as “classical ghost imaging in reverse”: rather than *measuring* intensity correlations to form a ghost image of an unknown object [26, 27, 30], one instead *establishes* such correlations to form a desired image. (iii) Figure 4 gives a discrete set of scan locations, but this could be changed to a continuous scan along a suitable path, with variable speed of traversal along such a path being used to deliver different doses at each

point on the path, in accord with Step #5 of the scheme in Sec. II A. (iv) Magnifying/de-magnifying geometries can be used. (v) Weighting coefficients (exposure times) for the random masks based on Eqs. (13) or (40) could be refined using optimization strategies such as Landweber iteration [39, 79], compressive sensing [78, 79], artificial neural networks [84] etc. (vi) A color version of the method is also possible. Recall that, when a thick diffusing screen is illuminated with a steady white light source, independent speckle fields are generated for a range of energy bands [85]. Hence, by replacing varying illumination times with varying illumination energy spectra, for a thick speckle-generating mask illuminated with statistically stationary white illumination, the method of the present paper could be adapted to the question of the projection of color images by spatially scanning a single spatially random screen. A thin spatially random screen could also be used to the same end, since the speckle patterns for different energy bands need not be different.

V. CONCLUSION

A means was outlined, for writing arbitrary intensity distributions, by transversely scanning a single spatially-random screen illuminated by a spatially but not necessarily temporally uniform radiation or matter wave-field. Two variants were developed, depending on whether or not correction was needed for the effects of Fresnel diffraction between the illuminated mask and the target illumination plane. The key idea for both variants was illustrated via computer simulation in two spatial dimensions. Some possible applications were discussed. All of this may be considered as a particular instance of the more general, and more generally applicable, idea of using random-function bases to “build signals out of noise”.

ACKNOWLEDGMENTS

The European Synchrotron (via Alexander Rack and Claudio Ferrero), the University of Christchurch (via Thomas Li and Konstantin Pavlov), the Swiss Light Source (via Anne Bonnin), the Technical University of Denmark (via Henning Poulsen), and the Technical University of Munich (via Kaye Morgan and Franz Pfeiffer) funded stimulating visits during which aspects of this manuscript were refined. Useful discussions are acknowledged, with Mario Beltran, Anne Bonnin, David Ceddia, Laura Clark, Michelle Croughan, Carsten Detlefs, Claudio Ferrero, Scott Findlay, Regine Gradl, Jean-Pierre Guigay, Timur Gureyev, Andrew Kingston, Alex Kozlov, Thomas Li, Gema Martínez-Criado, Jane Micallef, Kaye Morgan, Glenn Myers, Margie Olbinado, Konstantin Pavlov, Timothy Petersen, Henning Poulsen, Alexander Rack, James Saunderson, Hugh Simons, Marco Stamparoni and Imants Svalbe. Carsten Detlefs alerted the author to several means for generating x-ray speckle. Mario Beltran provided Fresnel-propagation code.

- [1] T. E. Gureyev, D. M. Paganin, A. Kozlov, Ya. I. Nesterets, and H. M. Quiney, *Phys. Rev. A* **97**, 053819 (2018).
- [2] A. Messiah, *Quantum Mechanics, volume 1* (North-Holland, Amsterdam, 1961).
- [3] S. Mallat, *A Wavelet Tour of Signal Processing: The Sparse Way*, 3rd ed. (Academic Press, Burlington, 2009).
- [4] Y.-L. Hsieh, G. T. Gullberg, G. L. Zeng, and R. H. Huesman, *IEEE Trans. Nucl. Sci.* **43**, 2306 (1996).
- [5] N. W. Ashcroft and N. D. Mermin, *Solid State Physics* (Thomson Learning, Singapore, 1976).
- [6] D. B. G. Spencer, *The Classical Orthogonal Polynomials* (World Scientific, Singapore, 2016).
- [7] R. N. Bracewell, *The Fourier Transform and its Applications*, 2nd ed. (McGraw-Hill Book Company, New York, 1986).
- [8] J. M. Cowley, *Diffraction Physics*, 3rd ed., Elsevier (Amsterdam, 1995).
- [9] B. E. A. Saleh and M. C. Teich, *Fundamentals of Photonics*, 2nd ed. (Wiley, New York, NY, 2007).
- [10] J. D. Jackson, *Classical Electrodynamics*, 3rd ed. (John Wiley & Sons, Hoboken, 1999).
- [11] W. A. Strauss, *Partial Differential Equations: An Introduction* (John Wiley & Sons, New York, 1992).
- [12] D. Ceddia and D. M. Paganin, *Phys. Rev. A* **97**, 062119 (2018).
- [13] A. N. Tikhonov and A. A. Samarskii, *Equations of Mathematical Physics* (Pergamon Press, Oxford, 1963).
- [14] I. L. Garanovich, S. Longhi, A. A. Sukhorukov, and Y. S. Kivshar, *Phys. Rep.* **518**, 1 (2012).
- [15] P. Zhidkov, *Nonlinear Anal. Theory Methods Appl.* **70**, 4123 (2009).
- [16] H. Stephani, *Differential Equations: Their Solution Using Symmetries* (Cambridge University Press, Cambridge, 1989).
- [17] B. H. Bransden and C. J. Joachain, *Introduction to Quantum Mechanics* (Longman Scientific & Technical, Essex, 1989).
- [18] Y. H. Gao and Y. F. Xing, *Compos. Struct.* **177**, 187 (2017).
- [19] A. Akhavi, J. Marckert, and A. Rouault, *ESAIM: Probab. Stat.* **13**, 437 (2009).
- [20] S. S. Vempala, *The Random Projection Method* (American Mathematical Society, Providence, Rhode Island, 2004).
- [21] A. N. Gorban, I. Y. Tyukin, D. V. Prokhorov, and K. I. Sofeikov, *Inf. Sci.* **364–365**, 129 (2016).
- [22] Y. Nakanishi-Ohno, T. Obuchi, M. Okada, and Y. Kabashima, *J. Stat. Mech.* **2016**, 063302 (2016).
- [23] L. Mandel and E. Wolf, *Optical Coherence and Quantum Optics* (Cambridge University Press, Cambridge, 1995).
- [24] S. Zelditch, *Phil. Trans. R. Soc. A* **372**, 20120511 (2014).
- [25] D. N. Klyshko, *Sov. Phys. J. E. T. P.* **67**, 1131 (1988).
- [26] Y. Bromberg, O. Katz, and Y. Silberberg, *Phys. Rev. A* **79**, 053840 (2009).
- [27] O. Katz, Y. Bromberg, and Y. Silberberg, *Appl. Phys. Lett.* **95**, 131110 (2009).
- [28] B. I. Erkmen and J. H. Shapiro, *Adv. Opt. Photonics* **2**, 405 (2010).
- [29] J. H. Shapiro and R. W. Boyd, *Quantum Inf. Process.* **11**, 949 (2012).
- [30] M. J. Padgett and R. W. Boyd, *Phil. Trans. R. Soc. A* **375**, 20160233 (2017).
- [31] M. F. Duarte, M. A. Davenport, D. Takhar, J. N. Laska, T. Sun, K. F. Kelly, and R. G. Baraniuk, *IEEE Signal Process. Mag.* **25**, 83 (March 2008).
- [32] M.-J. Sun, M. P. Edgar, G. M. Gibson, B. Sun, N. Radwell, R. Lamb, and M. J. Padgett, *Nat. Commun.* **7** (2016), article no. 12010.
- [33] F. Rousset, N. Ducros, A. Farina, G. Valentini, C. D’Andrea, and F. Peyrin, *IEEE Trans. Comput. Imaging* **3**, 36 (2017).
- [34] E. J. Candès and T. Tao, *IEEE Trans. Inf. Theory* **52**, 5406 (2006).
- [35] M. Rani, S. B. Dhok, and R. B. Deshmukh, *IEEE Access* **6**, 4875 (2018).
- [36] D. Achlioptas, *J. Comput. Syst. Sci.* **66**, 671 (2003).
- [37] N. V. Chawla and K. W. Bowyer, in *2005 IEEE Computer Society Conference on Computer Vision and Pattern Recognition (CVPR’05)*, Vol. 2 (2005) pp. 582–589 vol. 2.
- [38] F. Ferri, D. Magatti, L. A. Lugiato, and A. Gatti, *Phys. Rev. Lett.* **104**, 253603 (2010).
- [39] D. Pelliccia, M. P. Olbinado, A. Rack, A. M. Kingston, G. R. Myers, and D. M. Paganin, *IUCrJ* **5**, 428 (2018).
- [40] E. Hecht, *Optics*, 4th ed. (Addison-Wesley, 1998).
- [41] Equation (8) is spoken of as a “smoothed completeness relation” on account of its direct comparison with the completeness relation (closure relation) $\lim_{N \rightarrow \infty} \sum_{j=1}^N \psi_j^*(\mathbf{r})\psi_j(\mathbf{r}') = \delta(\mathbf{r} - \mathbf{r}')$ [1, 17]. Here, each member of a complete complex basis is denoted by ψ_j , \mathbf{r}, \mathbf{r}' are position vectors and δ denotes the Dirac delta. Dropping the star due to working with real functions, truncating the sum to a finite number of terms N , and replacing the Dirac delta with a mollified (smoothed) form that is nonetheless both peaked and normalized to unity, leads directly to Eq. (8). Here, the background-subtracted mask functions $\mathcal{M}_j(x, y) - \bar{\mathcal{M}}$ play the role of a random set of basis functions that are orthogonal in expectation value [12, 39].
- [42] M. Born and E. Wolf, *Principles of Optics*, 7th ed. (Cambridge University Press, Cambridge, 1999).
- [43] D. M. Paganin, *Coherent X-Ray Optics* (Oxford University Press, Oxford, 2006).
- [44] M. R. Teague, *J. Opt. Soc. Am.* **73**, 1434 (1983).
- [45] D. M. Paganin and D. Pelliccia, “Tutorials on x-ray phase contrast imaging: Some fundamentals and some conjectures on future developments,” (2019), arXiv:1902.00364.
- [46] D. Paganin, S. C. Mayo, T. E. Gureyev, P. R. Miller, and S. W. Wilkins, *J. Microsc.* **206**, 33 (2002).
- [47] F. W. J. Olver, D. W. Lozier, R. F. Boisvert, and C. W. Clark, eds., *NIST Handbook of Mathematical Functions* (Cambridge University Press, New York, 2010).
- [48] S. K. Sinha, E. B. Sirota, S. Garoff, and H. B. Stanley, *Phys. Rev. B* **38**, 2297 (1988).
- [49] S. C. Irvine, D. M. Paganin, S. Dubsy, R. A. Lewis, and A. Fouras, *Appl. Phys. Lett.* **93**, 153901 (2008).
- [50] S. C. Irvine, D. M. Paganin, A. Jamison, S. Dubsy, and A. Fouras, *Opt. Express* **18**, 2368 (2010).
- [51] I. Ng, D. M. Paganin, and A. Fouras, *J. Appl. Phys.* **112**, 074701 (2012).

- [52] T. E. Gureyev, A. W. Stevenson, D. M. Paganin, T. Weitkamp, A. Snigirev, I. Snigireva, and S. W. Wilkins, *J. Synchrotron Rad.* **9**, 148 (2002).
- [53] A. Snigirev, I. Snigireva, V. Kohn, S. Kuznetsov, and I. Schelokov, *Rev. Sci. Instrum.* **66**, 5486 (1995).
- [54] P. Cloetens, R. Barrett, J. Baruchel, J.-P. Guigay, and M. Schlenker, *J. Phys. D: Appl. Phys.* **29**, 133 (1996).
- [55] S. W. Wilkins, Ya. I. Nesterets, T. E. Gureyev, S. C. Mayo, A. Pogany, and A. W. Stevenson, *Phil. Trans. R. Soc. A* **372** (2014), article no. 20130021.
- [56] R. L. Easton Jr, *Fourier Methods in Imaging*, 6th ed. (Wiley, West Sussex, 2010).
- [57] J. M. C. Brown, J. E. Gillam, D. M. Paganin, and M. R. Dimmock, *IEEE Trans. Nucl. Sci.* **60**, 3333 (2013).
- [58] D. Eagleman, *Nat. Rev. Neurosci.* **2**, 920 (2001).
- [59] S. Wallis and M. Georgeson, *J. Vision* **12**, 1 (2010).
- [60] J. W. Goodman, *Speckle Phenomena in Optics* (Roberts and Company, Englewood Colorado, 2007).
- [61] S. Sanchez, P. E. Ahlberg, K. M. Trinajstic, A. Mirone, and P. Tafforeau, *Microsc. Microanal.* **18**, 1095 (2012).
- [62] S. C. Irvine, K. S. Morgan, Y. Suzuki, K. Uesugi, A. Takeuchi, D. M. Paganin, and K. K. W. Siu, *Opt. Express* **18**, 13478 (2010).
- [63] I. Aloisio, D. M. Paganin, C. Wright, and K. Morgan, *J. Synchrotron Radiat.* **22**, 1279 (2015).
- [64] Y. Matsuura, I. Yoshizaki, and M. Tanaka, *J. Appl. Cryst.* **37**, 841 (2004).
- [65] A. Goikhman, I. Lyatun, P. Ershov, I. Snigireva, P. Wajda, V. Gorlevsky, A. Semenov, M. Sheverdyayev, V. Koleskiy, and A. Snigirev, *J. Synchrotron Rad.* **22**, 796 (2015).
- [66] J. Bingi and V. M. Murukeshan, *Sci. Rep.* **5**, 18452 (2015).
- [67] J. C. H. Spence, *High-Resolution Electron Microscopy*, 4th ed. (Cambridge University Press, Cambridge, 2017).
- [68] A. C. Y. Liu, D. M. Paganin, L. Bourgeois, P. N. H. Nakashima, R. T. Ott, and M. J. Kramer, *Phys. Rev. B* **84**, 094201 (2011).
- [69] G. Song, J. Y. Y. Lin, J. C. Bilheux, Q. Xie, L. J. Santodonato, J. J. Molaison, H. D. Skorpenske, A. M. Dos Santos, C. A. Tulk, K. An, A. D. Stoica, M. M. Kirka, R. R. Dehoff, A. S. Tremsin, J. Bunn, L. M. Sochalski-Kolbus, and H. Z. Bilheux, *J. Imaging* **3**, 65 (2017).
- [70] F. H. Kim, D. Penumadu, J. Gregor, N. Kardjilov, and I. Manke, *J. Geotech. Geoenviron. Eng.* **139**, 715 (2013).
- [71] H. Bremmer, *Physica* **18**, 469 (1952).
- [72] B. E. Allman, P. J. McMahon, K. A. Nugent, D. Paganin, D. L. Jacobson, M. Arif, and S. A. Werner, *Nature* **408**, 158 (2000).
- [73] R. Fitzgerald, *Phys. Today* **53**, 23 (July 2000).
- [74] A. Bocolini, A. Fedrizzi, and D. Faccio, *Opt. Express* **27**, 9258 (2019).
- [75] G. Wang, H. Zheng, Y. Zhou, H. Chen, J. Liu, Y. He, Y. Yuan, F. Li, and Z. Xu, "All-optical naked-eye ghost imaging," (2019), arXiv:1904.06530.
- [76] G. Wang, H. Zheng, Y. Zhou, H. Chen, J. Liu, Y. He, Y. Yuan, F. Li, and Z. Xu, "Naked-eye ghost imaging via photoelectric-feedback," (2019), arXiv:1904.06529.
- [77] B. E. Kelly, I. Bhattacharya, H. Heidari, M. Shusteff, C. M. Spadaccini, and H. K. Taylor, *Science* **363**, 1075 (2019).
- [78] A. M. Kingston, G. R. Myers, D. Pelliccia, I. D. Svalbe, and D. M. Paganin, *Optica* **5**, 1516 (2018).
- [79] A. M. Kingston, D. Pelliccia, A. Rack, M. P. Olbinado, Y. Cheng, G. R. Myers, and D. M. Paganin, *IEEE Trans. Comput. Imaging* **5**, 136 (2019).
- [80] G. Ramachandran and A. Lakshminarayanan, *Proc. Natl. Acad. Sci. U. S. A.* **68**, 2236 (1971).
- [81] A. C. Kak and M. Slaney, *Principles of Computerized Tomographic Imaging* (IEEE Press, 1988).
- [82] T. E. Gureyev, D. M. Paganin, G. R. Myers, Ya. I. Nesterets, and S. W. Wilkins, *Appl. Phys. Lett.* **89**, 034102 (2006).
- [83] S. J. Pennycook and P. D. Nellist, eds., *Scanning Transmission Electron Microscopy: Imaging and Analysis* (Springer, 2011).
- [84] M. Lyu, W. Wang, H. Wang, H. Wang, G. Li, N. Chen, and G. Situ, *Sci. Rep.* **7**, 17865 (2017).
- [85] A. P. Mosk, A. Lagendijk, G. Lerosey, and M. Fink, *Nat. Photonics* **6**, 283 (2012).